Magnetorotational Effects on Anisotropic Neutrino Emission and Convection in Core Collapse Supernovae

Kei Kotake [1], Hidetomo Sawai [2], Shoichi Yamada [2], and Katsuhiko Sato [1,3]

[1] *Department of Physics, School of Science, University of Tokyo, 7-3-1 Hongo, Bunkyo, Tokyo 113-0033, Japan*

kkotake@utap.phys.s.u-tokyo.ac.jp

[2] *Science & Engineering, Waseda University, 3-4-1 Okubo, Shinjuku, Tokyo, 169-8555, Japan*

[3] *Research Center for the Early Universe, University of Tokyo, 7-3-1 Hongo, Bunkyo, Tokyo 113-0033, Japan*

ABSTRACT

We perform a series of two-dimensional hydrodynamic simulations of the magnetorotational collapse of a supernova core. We employ a realistic equation of state and take into account electron capture and neutrino transport by the so-called leakage scheme. Recent stellar evolution calculations imply that the magnetic fields of the toroidal components are much stronger than the poloidal ones at the presupernova stage. In this study, we systematically investigate the effects of the toroidal magnetic fields on the anisotropic neutrino radiation and convection. Our results show that the shapes of the shock wave and the neutrino spheres generally become more oblate for the models whose profiles of rotation and magnetic field are shell-type, in contrast, more prolate for the models whose profiles of rotation and magnetic field are cylindrical, than the corresponding models without the magnetic fields. Furthermore, we find that the magnetorotational instability induced by the nonaxisymmetric perturbations is expected to develop within the prompt shock timescale. Combined with the anisotropic neutrino radiation, which heats matter near the rotational axis preferentially, the growth of the instability may enhance the heating near the axis. This might suggest that the magnetar formation is accompanied by the jet-like explosion.

Subject headings: supernovae: collapse, rotation—magnetars: pulsars, magnetic field

1. Introduction

Recent numerical studies of core collapse supernovae in spherical symmetry have developed so far as to handle elaborate neutrino transports, detailed microphysics and/or general relativity. However, most of the spherical models have failed to produce explosions (Rampp & Janka 2000; Liebendörfer et al. 2001; Thompson, Burrows, & Pinto 2003; Liebendörfer et al. 2003). In the meantime, there are accumulating observations, which require the revision of the spherically symmetric stellar collapse. Spectropolarimetric observations have commonly shown a percent level of linear polarization, which may be interpreted as the asymmetry of core collapse supernovae (Wang et al. 1996, 2001). It is also well known that SN 1987 A is globally asymmetric, which is directly observed by *Hubble Space Telescope* (Pun et al. 2001; Wang et al. 2002). These situations have attracted some physicists to revisit macroscopic effects such as rotation and/or magnetic field on the explosion mechanism itself or on the gravitational radiation (Akiyama et al. 2003; Buras et al. 2003; Kotake et al. 2003; Ott et al. 2003; Kotake et al. 2003; Fryer & Warren 2003; Müller et al. 2003).

In the previous paper, we did 2D rotational core collapse simulations and estimated the anisotropy of neutrino radiation (Kotake et al. 2003). As a result, we found that neutrinos heat matter near the rotational axis more strongly than in the vicinity of the equatorial plane. This anisotropic neutrino radiation induced by rotation might produce a jet like explosion as suggested by the observations of SN1987A (Shimizu et al. 2001). It should be also mentioned that the jet like explosion plays important roles in the nucleosynthesis of heavy elements (Nagataki, Hashimoto, Sato, & Yamada 1997; Nagataki 2000). This paper is a sequel of Kotake et al. (2003). We take into account magnetic field and investigate its effect on the anisotropic neutrino radiation as well as convection.

The number of magnetohydrodynamic simulations done so far is very small (LeBlanc & Wilson 1970; Bisnovatyi-Kogan et al. 1976; Meier et al. 1976; Müller & Hillebrandt 1979; Symbalisty 1984; Ardeljan et al. 2000; Yamada & Sawai 2003) in comparison with the spherically symmetric models. Most serious of them is probably the study by Symbalisty (1984). He employed a realistic EOS and treated neutrino transfer by a flux-limited diffusion scheme. He found that an explosion occurs only when the star rotates very fast and has extremely strong magnetic field $\sim 10^{16}$ G at the surface of the protoneutron star. The value is almost $2 \sim 3$ orders of magnitudes greater than the canonical one observed for pulsars.

In most of the preceding papers, it was assumed that the initial magnetic field is uniform and parallel to the rotational axis (see, however, Ardeljan et al. 2000) in which dipole and quadrupole magnetic fields were studied. On the other hand, recent stellar evolution studies show that the toroidal field components may be stronger than the poloidal ones prior to the collapse (Heger et al. 2003; Spruit 2002). In this study, we perform a series of 2D simulations

of magnetorotational core collapse changing the strength of rotation and toroidal magnetic fields systematically. By doing so, we hope to understand the effect of toroidal magnetic fields on the anisotropic radiation and convection both in the weak magnetic field ($\sim 10^{12}$ G) regime and in the strong magnetic field ($\sim 10^{15}$ G) regime at the formation of protoneutron star. The latter case may be associated with the formation of the so-called magnetars (Duncan & Thompson 1992), such as anomalous X-ray pulsars and soft gamma-ray repeaters (Zhang & Harding 2000; Guseinov et al. 2003). Although the number of the magnetars is much smaller in comparison with the canonical pulsars, their origin and formation mechanism should be explained.

We describe the numerical methods in section 2. The main numerical results are shown in section 3. Discussions are given in section4. We conclude this paper in section 5.

2. Numerical Methods

The numerical method for MHD computations employed in this paper is based on the ZEUS-2D code (Stone & Norman 1992). The basic evolution equations are written as follows,

$$\frac{d\rho}{dt} + \rho\nabla\cdot\boldsymbol{v} = 0, \tag{1}$$

$$\rho\frac{d\boldsymbol{v}}{dt} = -\nabla P - \rho\nabla\Phi + \frac{1}{4\pi}(\nabla\times\boldsymbol{B})\times\boldsymbol{B}, \tag{2}$$

$$\rho\frac{d\left(\frac{e}{\rho}\right)}{dt} = -P\nabla\cdot\boldsymbol{v}, \tag{3}$$

$$\frac{\partial\boldsymbol{B}}{\partial t} = \nabla\times(\boldsymbol{v}\times\boldsymbol{B}) \tag{4}$$

$$\Delta\Phi = 4\pi G\rho, \tag{5}$$

where $\rho, \boldsymbol{v}, e, P, \boldsymbol{B}, \Phi$ are density, velocity, internal energy, pressure, magnetic field, and gravitational potential, respectively. We denote the Lagrangian derivative as d/dt . The ZEUS-2D is an Eulerian code based on the finite-difference method and employs an artificial viscosity of von Neumann and Richtmyer to capture shocks. The time evolution of magnetic field is solved by the induction equation, Eq. (4). In so doing, the code utilizes the so-called constrained transport (CT) method, which ensures the divergence free ($\nabla\cdot\boldsymbol{B} = 0$) of the numerically evolved magnetic fields at all times. Furthermore, the method of characteristics (MOC) is implemented to propagate accurately all modes of MHD waves. The self-gravity is managed by solving the Poisson equation with the incomplete Cholesky decomposition conjugate gradient method. In all the computations, spherical coordinates are used and one

quadrant of the meridian section is covered with 300 (r) $\times$ 50 (θ) mesh points. We have made several major changes to the base code to incorporate the microphysics. First, we added an equation for the electron fraction to treat electron captures and neutrino transport by the so-called leakage scheme (Epstein & Pethick 1981; Bludman et al. 1982; Van Riper & Lattimer 1981; Van Riper 1982). The calculation of electron fraction is done separately from the main hydrodynamic step in an operator-splitting manner. Second, we implemented a tabulated equation of state based on the relativistic mean field theory (Shen et al. 1998) instead of the ideal gas EOS assumed in the original code. For a more detailed description of the methods, see Kotake et al. (2003).

3. Numerical Results

3.1. Initial Conditions

Recently, Heger et al. (2003) performed the stellar evolution calculations in which rotation and magnetic fields are taken into account. Remembering caveats that their calculations are based on the one-dimensional models with uncertainties and not the final answer probably, they pointed out that the toroidal components of the magnetic fields are stronger than the poloidal ones at the presupernova stage. It is because the differential rotation amplifies the toroidal components by a convective stellar dynamo during the quasistatic stellar evolution (e.g., Parker 1979; Spruit 2002). To our knowledge, past MHD simulations for core collapse supernovae chosen poloidal magnetic fields as the initial conditions. This situation motivates us to take the initial conditions in which the toroidal components are dominant over the poloidal ones. Since Heger et al. (2003) calculated only a small set of models so far, we prefer a parametric approach to construct the initial conditions in this paper.

We assume the following two rotation laws. In addition, we prepare the toroidal magnetic fields to yield the same profile as the rotation.

1. shell-type profile:

$$\Omega(r) = \Omega_0 \times \frac{{R_0}^2}{r^2 + R_0^2}, \tag{6}$$

$$B_\phi(r) = B_0 \times \frac{{R_0}^2}{r^2 + R_0^2}, \tag{7}$$

where $\Omega(r)$ is angular velocity, $B_\phi(r)$ is toroidal component of the magnetic fields, r is radius, and Ω_0, R_0 are model constants,

2. cylindrical profile:

$$\Omega(X,Z) = \Omega_0 \times \frac{{X_0}^2}{X^2 + {X_0}^2} \cdot \frac{Z_0^4}{Z^4 + Z_0^4}, \tag{8}$$

$$B_\phi(X,Z) = B_0 \times \frac{{X_0}^2}{X^2 + {X_0}^2} \cdot \frac{Z_0^4}{Z^4 + Z_0^4}, \tag{9}$$

where X and Z denote distances from the rotational axis and the equatorial plane, and X_0, Z_0 are model constants. The other parameters have the same meanings as above.

We have computed ten models changing the combination of the total angular momentum, the rotation profile, the degree of differential rotation and the total magnetic energy. The model parameters are presented in Table 1. The models are named after the combination, with the first letter, "S (slow)", "M (moderate)", representing the initial $T/|W|$, the second letter "S (shell-type)", "C (cylindrical)", denoting the rotation profiles, the third letter, "L (long)", "S (short)", indicating the values of R_0, Z_0, which represent the degree of differential rotation, and the fourth letter, "7 $\sim$ 1", indicating the value of $E_{\rm m}/|W|$. It is noted the ratio of magnetic and rotational energy to gravitational energy are designated as $E_{\rm m}/|W|$ and $T/|W|$, respectively. We have chosen $\sim 10^{-3}, 0.5\%$ for the initial $T/|W|$ and $10^{-7}, 10^{-4}, 10^{-2}, 10^{-1}\%$ for the initial $E_{\rm m}/|W|$. The initial poloidal components of the magnetic fields are assumed to be uniform and parallel to the rotation axis, whose value is taken to be about four orders of magnitude lower than the toroidal components in accordance with the results by Heger et al. (2003). We have made precollapse models by taking a density, internal energy, electron fraction distributions from the spherically symmetric $15M_\odot$ model by Woosley&Weaver (1995) and adding the angular momentum and the magnetic fields according to the prescription stated above.

Heger et al. (2003) pointed out that the iron core may rotate more slowly with the magnetic fields than without. It is because the magnetic braking reduces the angular momentum of the core during the quasistatic stellar evolution. Model SSL7 corresponds to the magnetorotational progenitor by Heger et al. (2003) and is chosen to study the effect of magnetic field in the weak field strength regime ($\sim 10^{12}$ G) at the formation of the protoneutron star. This is the case for the formation of the canonical pulsars. On the other hand, other models are prepared to study the formation of the so-called magnetars.

Table 1. The Model Parameters.

Model	$T/\|W\|(\%)$	$E_{\rm m}/\|W\|(\%)$	Rotation Law	R_0, X_0, Z_0 $\times 10^8$ (cm)	Ω_0 (s^{-1})	B_0 (G)
SSL7	3.2×10^{-3}	9.7×10^{-8}	Shell-type	$R_0=1$	0.1	5.0×10^{9}
MSL4	5.0×10^{-1}	10^{-4}	Shell-type	$R_0=1$	4.0	1.6×10^{11}
MSL2	5.0×10^{-1}	10^{-2}	Shell-type	$R_0=1$	4.0	1.6×10^{12}
MSL1	5.0×10^{-1}	10^{-1}	Shell-type	$R_0=1$	4.0	5.0×10^{12}
MSS4	5.0×10^{-1}	10^{-4}	Shell-type	$R_0=0.1$	63.4	3.5×10^{12}
MSS2	5.0×10^{-1}	10^{-2}	Shell-type	$R_0=0.1$	63.4	3.5×10^{13}
MSS1	5.0×10^{-1}	10^{-1}	Shell-type	$R_0=0.1$	63.4	1.1×10^{14}
MCS4	5.0×10^{-1}	10^{-4}	Cylindrical	$X_0=0.1, Z_0=1$	44.4	1.5×10^{12}
MCS2	5.0×10^{-1}	10^{-2}	Cylindrical	$X_0=0.1, Z_0=1$	44.4	1.5×10^{13}
MCS1	5.0×10^{-1}	10^{-1}	Cylindrical	$X_0=0.1, Z_0=1$	44.4	4.8×10^{13}

Table 2. Important Quantities at Core Bounce.

Model	$t_{\rm b}$ (ms)	$\rho_{\rm maxb}(10^{14}{\rm g\ cm^{-3}})$	$M_{\rm in,b}(M_\odot)$	$T/\|W\|_{\rm b,in}(\%)$	$T/\|W\|_{\rm b,out}(\%)$	$E_{\rm m}/\|W\|_{\rm b,in}(\%)$	$E_{\rm m}/\|W\|_{\rm b,out}(\%)$
SSL7	214.6	2.97	0.61	8.0×10^{-3}	1.4×10^{-2}	2.4×10^{-8}	2.6×10^{-8}
MSL4	242.8	2.61	0.83	9.4	20.8	4.2×10^{-5}	4.0×10^{-5}
MSL2	242.9	2.66	0.83	9.5	20.8	4.2×10^{-3}	3.9×10^{-3}
MSL1	242.7	2.65	0.83	9.5	20.7	3.9×10^{-2}	3.6×10^{-2}
MSS4	241.8	1.72	0.87	11.2	9.4	4.8×10^{-4}	7.7×10^{-5}
MSS2	242.0	1.71	0.87	11.0	9.4	4.2×10^{-2}	8.0×10^{-4}
MSS1	242.1	2.10	0.87	11.3	9.4	3.4×10^{-1}	7.8×10^{-3}
MCS4	245.4	1.45	0.91	12.4	6.4	3.8×10^{-4}	1.3×10^{-4}
MCS2	244.1	1.55	0.91	12.4	6.5	3.4×10^{-2}	1.2×10^{-2}
MCS1	244.2	1.88	0.91	12.5	6.5	2.3×10^{-1}	6.0×10^{-2}

Note. — $t_{\rm b}$, $\rho_{\rm maxb}$, and $M_{\rm in,b}$ are the time, the central density, and the inner core mass at bounce, respectively. $T/|W|$, $E_{\rm m}/|W|$ are the ratios of the rotational and magnetic energy to the gravitational energy, respectively. The subscript $_{\rm b}$ implies the values at bounce, $_{\rm in}$ and $_{\rm out}$ represent the values in the inner core and outer core. Note that we speak of the inner and outer cores, in which matters fall subsonically and supersonically, respectively.

Table 3. Properties of the Final States.

Model	$t_{\rm f}$ (ms)	$r_{\rm sh}^{\rm e}$ (km)	$r_{\rm sh}^{\rm p}$ (km)	R	$\rho_{\rm c}$ (10^{14} g cm^{-3})	$B_{\rm c}$ (G)	$\Omega_{\rm max}$ (s^{-1})	$T/\|W\|_{\rm f}$(%)	$E_{\rm m}/\|W\|_{\rm f}$(%)
SSL7	254.4	160	160	1.0	2.77	1.2×10^{13}	5.4×10^{4}	1.0×10^{-2}	3.5×10^{-8}
MSL4	287.2	220	170	0.8	1.49	2.9×10^{14}	7.5×10^{5}	8.7	4.3×10^{-5}
MSL2	286.1	230	150	0.7	1.52	2.7×10^{15}	9.1×10^{5}	8.6	4.2×10^{-3}
MSL1	287.0	220	160	0.7	1.35	7.7×10^{15}	3.1×10^{5}	8.6	3.9×10^{-2}
MSS4	286.8	220	250	1.1	1.34	4.1×10^{15}	9.3×10^{4}	9.0	2.9×10^{-4}
MSS2	286.7	220	250	1.1	1.52	4.9×10^{16}	8.8×10^{4}	9.0	2.9×10^{-2}
MSS1	286.9	230	270	1.2	1.66	1.5×10^{17}	1.0×10^{5}	9.1	2.4×10^{-1}
MCS4	290.3	400	400	1.0	0.66	3.7×10^{15}	8.8×10^{4}	9.9	3.0×10^{-4}
MCS2	290.2	410	430	1.0	0.82	4.0×10^{16}	4.5×10^{4}	10.0	2.7×10^{-2}
MCS1	291.8	460	650	1.4	1.08	8.4×10^{16}	5.9×10^{4}	10.1	1.8×10^{-1}

Note. — $r_{\rm sh}^{\rm e}$ and $r_{\rm sh}^{\rm p}$ are the distances from the center to the stalled shock front in the equatorial plane and along the rotational axis, respectively. R is the aspect ratio of the shock wave, that is, $R = {r_{\rm sh}}^{\rm p}/{r_{\rm sh}}^{\rm e}$. Subscript $_{\rm f}$ implies the values at the final states. $\rho_{\rm c}$ and $B_{\rm c}$ are the central density and the strength of the magnetic field. Note that $T/|W|$ and $E_{\rm m}|W|$ in this table are the values integrated over the whole core.

3.2. The Hydrodynamic Features in Magnetorotational Core Collapse

We will first summarize some dynamical aspects in order to characterize differences among models, which will be necessary in the later discussions.

In all the models, the shock wave produced by core bounce stalls in the core and no prompt explosion occurs. The final time of all the models is about 50 msec after core bounce. In Figures 1 and 2, the entropy and the magnetic field distributions at the final states for some representative models are presented, respectively. A variety of final shapes is immediately seen in these figures. The properties at the core bounce and the final states are summarized in Tables 2 and 3. Note that the high entropy regions in Figure 1 are formed by the shock heating, since our calculations include only neutrino cooling but exclude the neutrino heating.

We first pay attention to the aspect ratio of the stalled shock, R. The values of R are smaller for the models with weak differential rotation (see Table 3 and compare the models whose name has "L" and "S" in the third letter). We take as an example the pair of models, MSL4 (weaker differential rotation) and MSS4 (stronger differential rotation), and see the difference of the dynamical behaviors between them. Then we investigate how the shapes of the shock waves are changed by the inclusion of the toroidal magnetic fields, by comparing the models in this study with the corresponding models but without the magnetic fields (e.g., Kotake et al. 2003).

Model MSL4 bounces at $t = 243$ msec at a central density of $2.6 \cdot 10^{14}$g cm^{-3}. It occurs at the pole first (see the left panel of Figure 3) around the radius of $\sim$ 20 km. Then, the high entropy blob ($\sim 9.5 k_B$/nucleon) formed at the pole by the core bounce begins to move upwards along the rotational axis by buoyancy. The shock wave stalls at $\sim$ 150km near the pole by the neutrino cooling and the ram pressure of the infalling matter. The shape of the shock wave is rather prolate in the beginning, and becomes oblate after the shock-stall due to the centrifugal force (see the upper right panel of Figure 1). Model MSS4 bounces at $t = 242$ msec at a central density of $1.7 \cdot 10^{14}$g cm^{-3}. The shock wave emerges at the radius of $\sim$ 20km not at the pole as in model MSL4 but rather like a shell (see the right panel of Figure 3). The high entropy shell $\sim 8.5 k_{\rm B}$/nucleon is formed afterwards. The shock wave at core bounce propagates keeping the aspect ratio and stalls finally (see the lower left panel of Figure 1). Next we discuss how the shapes of the shock wave are changed by the inclusion of the toroidal magnetic fields. For the models whose profiles of rotation and the magnetic field are shell-type, the shapes tend to become more oblate by the toroidal magnetic fields. As for the above pair, the value of R is 0.8 for model MSL4, in contrast, 1.0 for the corresponding model without the magnetic fields, and 1.1 for model MSS4, in contrast, 1.9

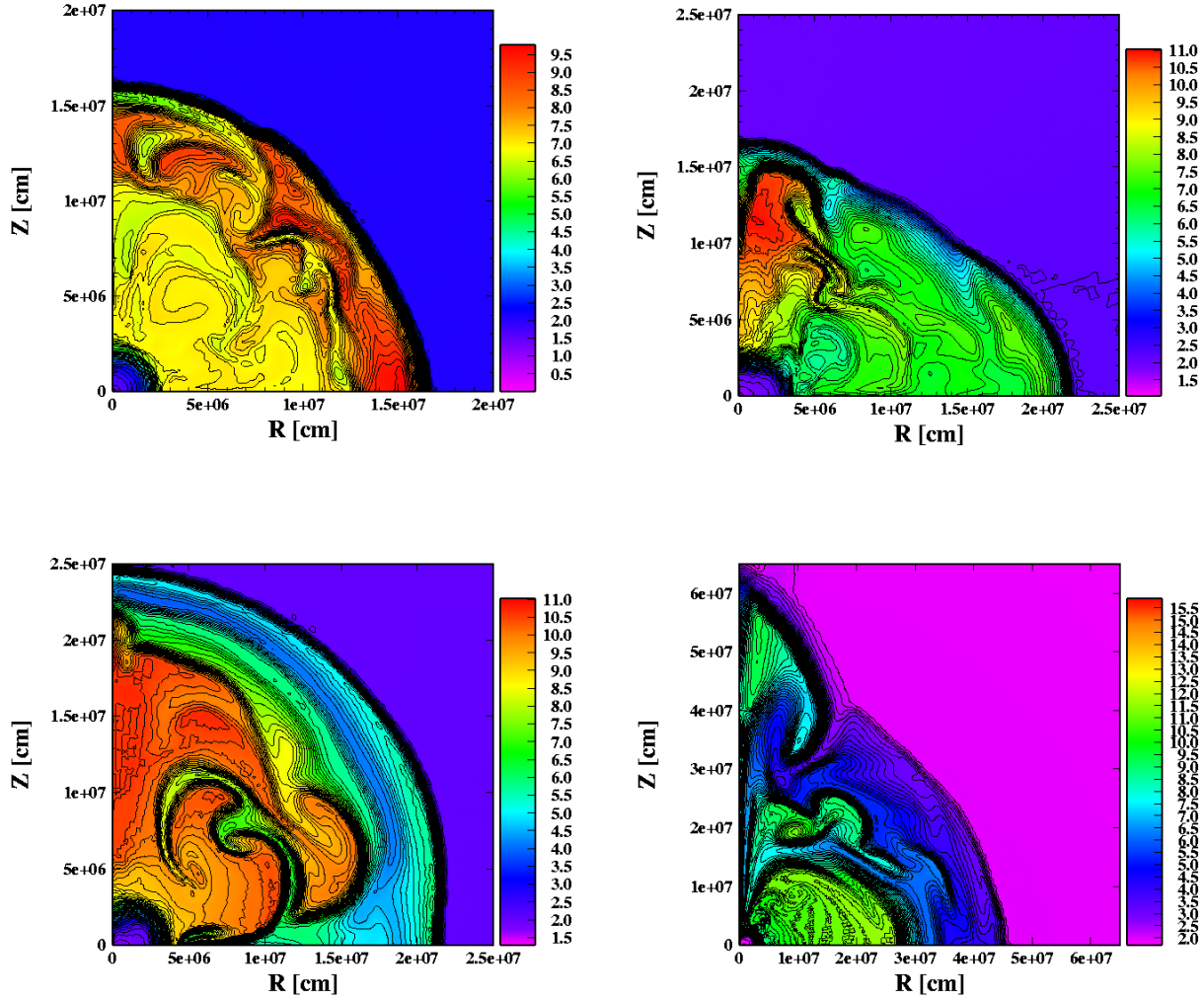

Fig. 1.— The final profiles of models SSL7 (upper left), MSL4 (upper right) MSS4 (lower left) and MCS1 (lower right). They show color-coded contour plots of entropy (k_B) per nucleon.

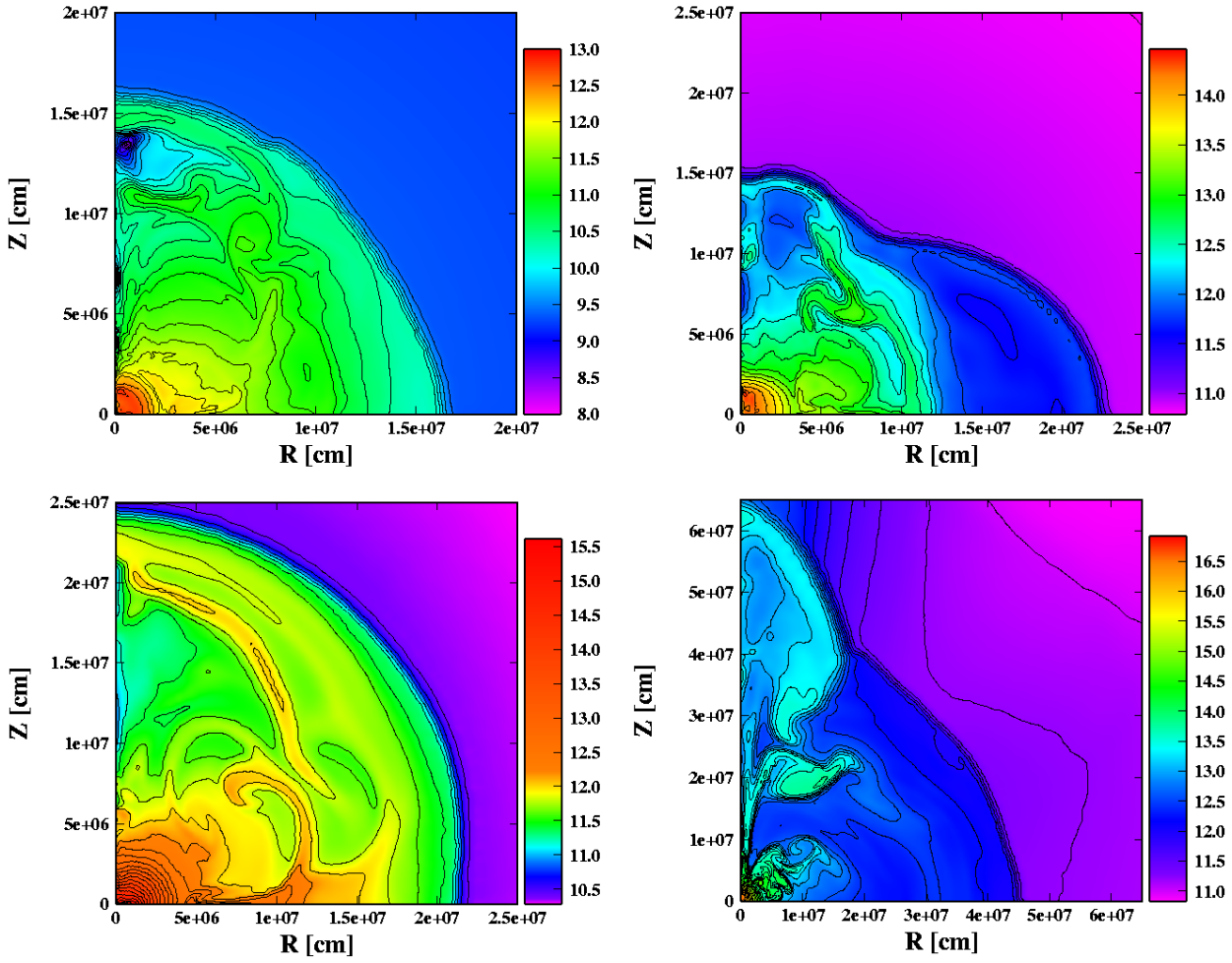

Fig. 2.— Same as Figure 1 but for the logarithm of the toroidal magnetic field : B_ϕ (G).

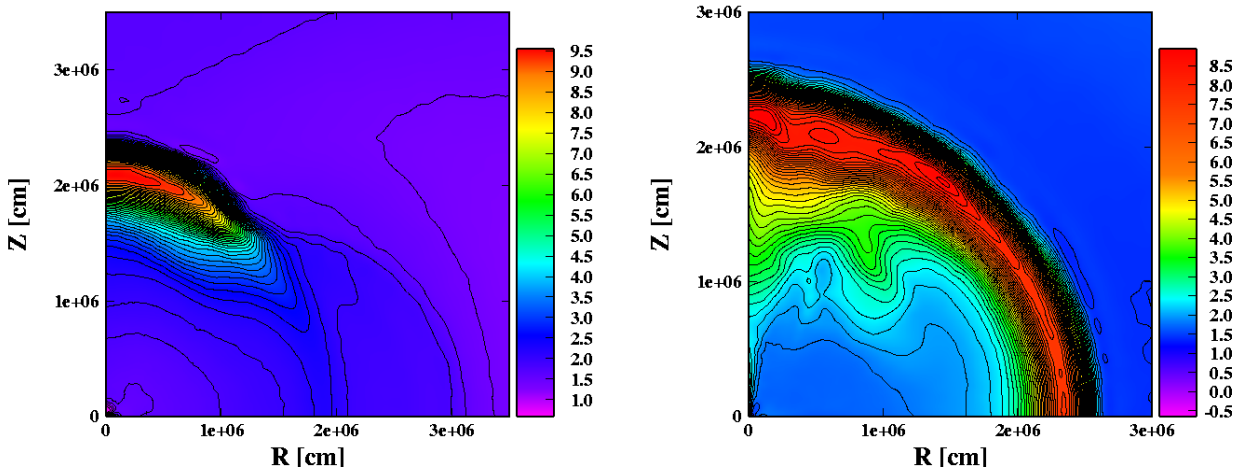

Fig. 3.— The entropy profiles at core bounce for models MSL4 (left panel) and MSS4 (right panel). They show color-coded contour plots of entropy (k_B) per nucleon.

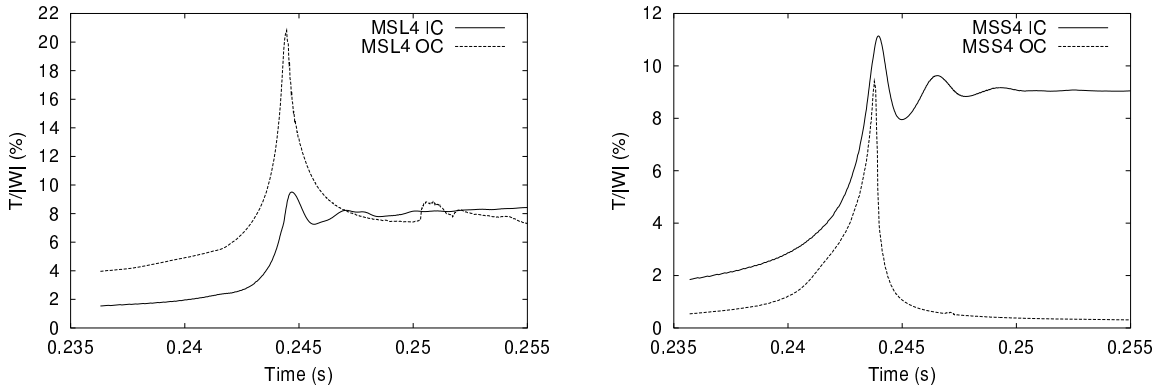

Fig. 4.— The time evolution of $T/|W|$ (%) near core bounce for models MSL4 (left panel) and MSS4 (right panel), respectively. IC and OC in the figures represents the inner and outer core, respectively.

for the corresponding model without the magnetic fields (for the models without magnetic fields, see Kotake et al. (2003)). The toroidal magnetic fields with the shell-type rotation pushes the matter rather parallel to the equatorial plane. In fact, the toroidal magnetic fields are concentrated rather in the vicinity of the equatorial plane, as seen the upper right and lower left panels of Figure 2. On the other hand, the shock wave becomes more prolate, for the models whose profiles of rotation and magnetic field are cylindrical. In fact, the values of R in the models whose names consist of MCS in this study are equal or greater than that of the corresponding model without the magnetic fields (e.g., Kotake et al. 2003). As seen from the toroidal magnetic fields profile of MCS1 (see the lower right panel of Figure 2), the magnetic fields are confined to the small region behind the shock wave. In addition, the magnetic fields pushes the shock wave, which acts as strong as the matter pressure. In the region, the ratio of the magnetic to matter pressure becomes as high as 90% for the model.

In Figure 4, the time evolutions of $T/|W|$ for the above pair (models MSL4 and MSS4) are presented. At core bounce, model MSL4 gives larger $T/|W|$ in the outer core in contrast with model MSS4, which gives larger $T/|W|$ in the inner core (compare the left with the right panels in Figure 4). It is due to the degree of the initial differential rotation. Similarly, due to the degree of the initial magnetic field concentration, $E_{\rm m}/|W|$ in the outer core for model MSL4 dominates over that in the inner core, while vice versa for model MSS4 (see Figure 5). These features are common to the other pairs (see Table 2).

Model SSL7 corresponding to the Heger's model bounces at $t = 215$ msec at a central density of $3.0 \cdot 10^{14}$g cm^{-3} and the shock wave stalls at a radius of 150 km. The strength of the magnetic fields at the surface of the protoneutron star becomes as high as $\sim 10^{12}$G (see the upper left panel of Figure 2). This value agrees with the canonical value of ordinary pulsars. The global hydrodynamic quantities at the final state, such as the radius at the

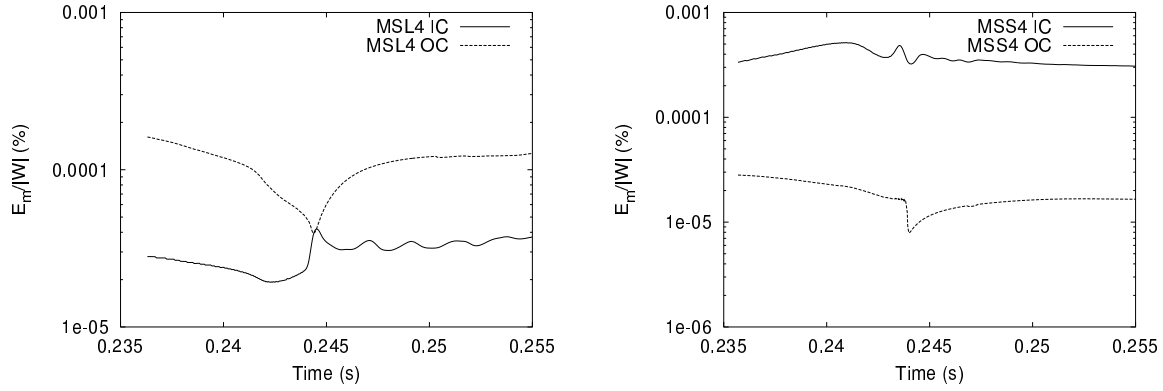

Fig. 5.— Same as Figure 4 but for $E_{\rm m}/|W|$ (%).

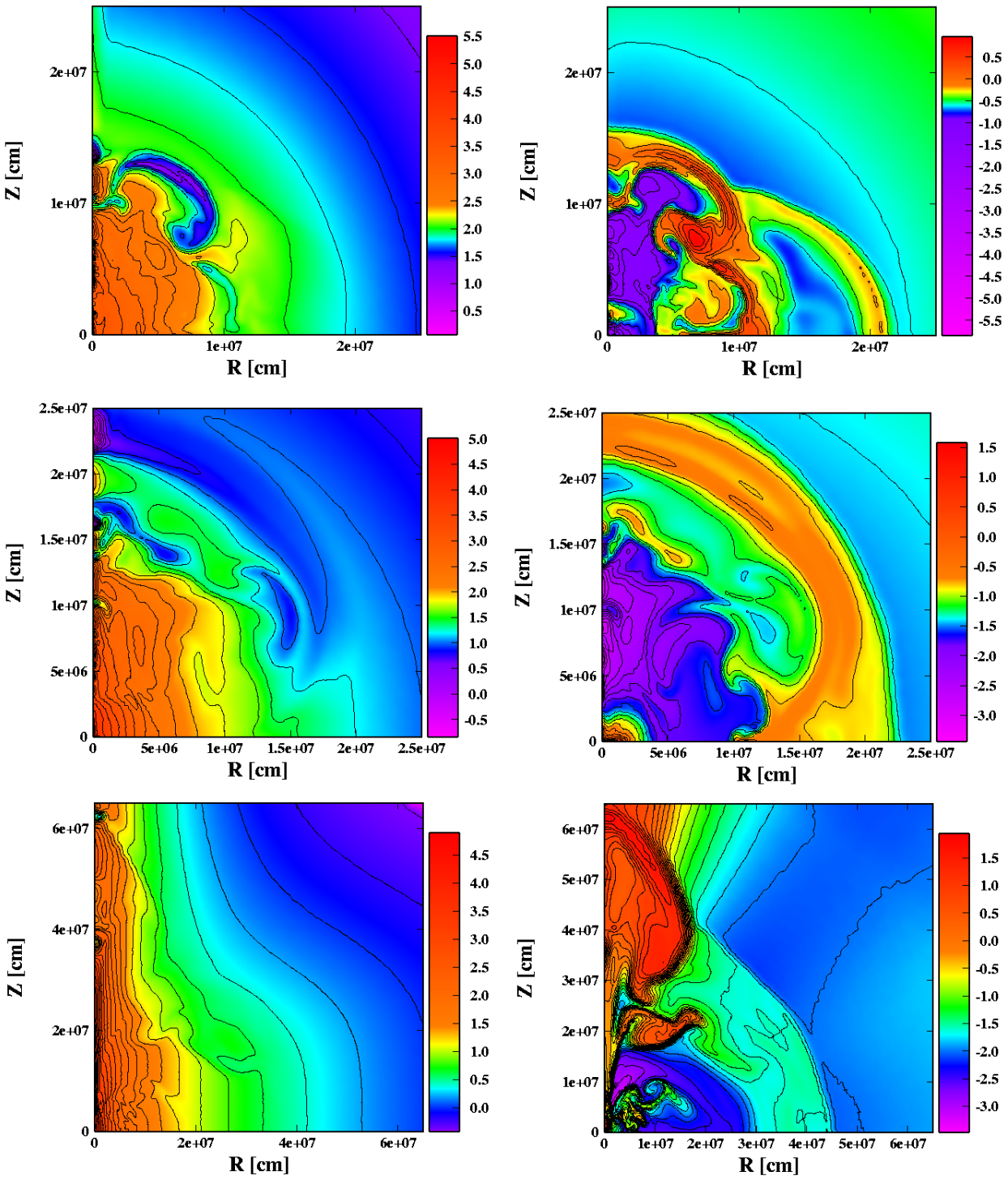

Fig. 6.— The contour plots for the logarithm of the angular velocity : Ω (s^{-1}) (left side of the panels) and of the ratio of magnetic pressure to matter pressure : $(B^2/8\pi)/p$ in percentage (right side of the panels) for models MSL1 (top), MSS1 (middle), and MCS1 (bottom).

shock-stall and the aspect ratio of the shock wave, resemble the spherical model in Kotake et al. (2003). The initial rotation rate and magnetic field in the recent stellar evolution calculation are not large enough to make the dynamics substantially deviated from being spherically symmetric. However, the convectively unstable regions are changed in model SSL7 compared with the spherical model. This will be discussed again in section 3.5.

Finally we mention some important features in the models with the strongest magnetic fields in our computations. In Figure 6, the contour plots of the angular velocity (left panels) and the ratio of magnetic to matter pressure (right panels) are presented for the models MSL1, MSS1, and MCS1. From the left side panels of Figure 6, the angular velocity distributions behind the shock wave are found to be cylindrical, although the initial rotation profiles for the models MSL1 and MSS1 are shell-type. It is noted that the rearrangement of the angular momentum distribution is caused by rotation (e.g., Tassoul (1978)). In our models, the magnetic fields cannot transfer the angular momentum because the magnetic fields are almost purely toroidal with the assumption of axial symmetry. From the right side panels of Figure 6, it is found that the ratio of magnetic to matter pressure behind the shock wave for the strong differential rotation models becomes more larger than that of the weak differential rotation model (compare the middle and bottom panels with the top panel with that of in the right side). In fact, the values of $E_{\rm m}/|W|$ becomes as large as $\sim 30\%$ ($B_\phi \sim 10^{11}$ G) for model MSS1 and $\sim 90\%$ ($B_\phi \sim 10^{13}$ G) for model MCS1 near the rotational axis (see Figures 2 and 6). Since the shock wave can reach further out for the models, the matter pressure behind the shock becomes relatively small, which makes the ratio larger.

In the next section, we proceed to analyze the neutrino spheres and estimate the degree of anisotropic neutrino radiation, based on the anisotropic matter distribution after the shock stagnation by the magnetohydrodynamic simulations.

3.3. Neutrino Emissions from the deformed Neutrino Spheres

3.3.1. The Shapes of Neutrino Sphere.

Following the common practice, we define the neutrino sphere, R_ν, as the radius satisfying the condition:

$$\int_{R_\nu}^{\infty} \frac{dr}{\lambda_{\rm tot}} = \frac{2}{3}. \tag{10}$$

In estimating $\lambda_{\rm tot}$, we consider the three dominant opacity sources for electron neutrino, that is, coherent scattering on nuclei, scattering on free nucleons, and absorption on neutrons (see

Kotake et al. (2003)). We perform the integration along the radius for each angular bin to obtain $R_\nu(\theta)$ as a function of the polar angle. Since neutrino reactions are highly dependent on the neutrino energy, the positions of the neutrino sphere are also energy-dependent. For the realistic estimation, we should distinguish the last scattering surface from that of last energy exchange. However, we stick to this rough approximation for simplicity in this study.

In Figure 7, the neutrino spheres for some representative models are presented. Comparing the spherical model without rotation and magnetic fields computed in Kotake et al. (2003) with model SSL7, we find no significant differences in the shapes and positions of the neutrino sphere. Therefore, if the rotational progenitor model by Heger et al. (2003) is true, no substantial deformation in the neutrino sphere is expected at least in the prompt-shock time scale.

Next we make comparison of the remaining models. As the final shapes of the shock wave are affected by the magnetic fields, the shapes of the neutrino sphere become more oblate by the magnetic fields for the models whose profiles of rotation and magnetic field are shell-type. On the other hand, the shapes become more prolate for the models whose profiles of rotation and magnetic field are cylindrical. However, the deformation of the neutrino spheres by the magnetic fields is found to be small. Thus, the shapes are found to be predominantly determined by rotation over the wide range of the initial field strength. The gloss features of the shapes seen in the case of pure rotation (see Kotake et al. (2003)) are also common to this study. That is to say, the neutrino sphere is deformed to be oblate due to the centrifugal force for the models with the shell-type rotation law (see MSL4, MSL1, MSS4, and MSS1 in Figure 7). The positions of the neutrino spheres on the equatorial plane move inwards (compare models MSS4, MSS1, MCS4 with the others in Figure 7) for the models with stronger differential rotations. This is because the matter on the equatorial plane is more condensed in the center region due to the strong differential rotation in which matter in the outer region falls more rapidly. The neutrino spheres are deformed to be cylinder like except for the dip in the polar region for the models with the cylindrical rotation profile (see MCS4 in Figure 7). The dip along the rotational axis arises because the density tends to be smaller along the rotational axis for these models. This is because the collimated shock propagates along the axis, sweeping out the matter near the region.

The temperature profile on the neutrino sphere for the representative models is presented in Figure 8. Although the profiles in the figure are not smooth due to the rather poor angular resolution in this study, it can be seen that the neutrino temperature varies with the polar angle and is generally higher at the rotational axis (see Figure 8). This is because the neutrino spheres are formed at smaller radii near the axis as seen from the shapes of neutrino sphere.

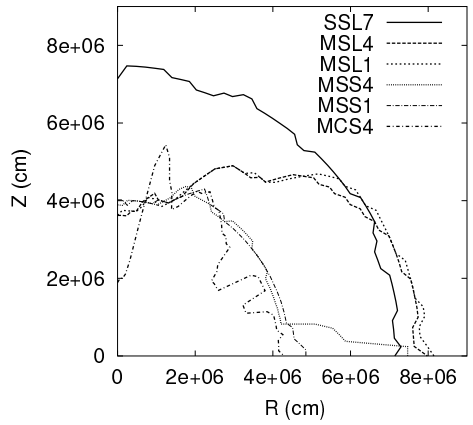

Fig. 7.— The shapes of neutrino sphere for the representative models.

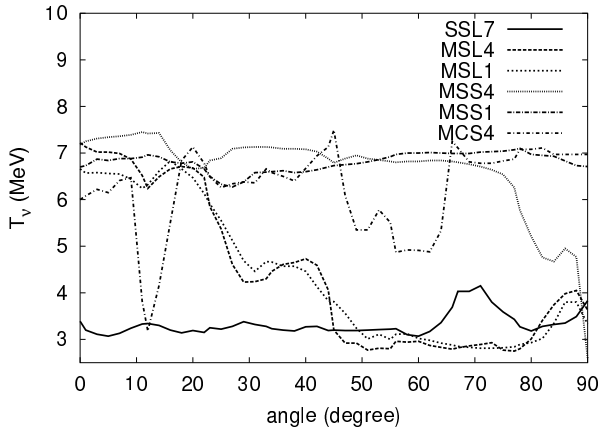

Fig. 8.— The neutrino temperatures with the polar angle on the neutrino sphere for the representative models.

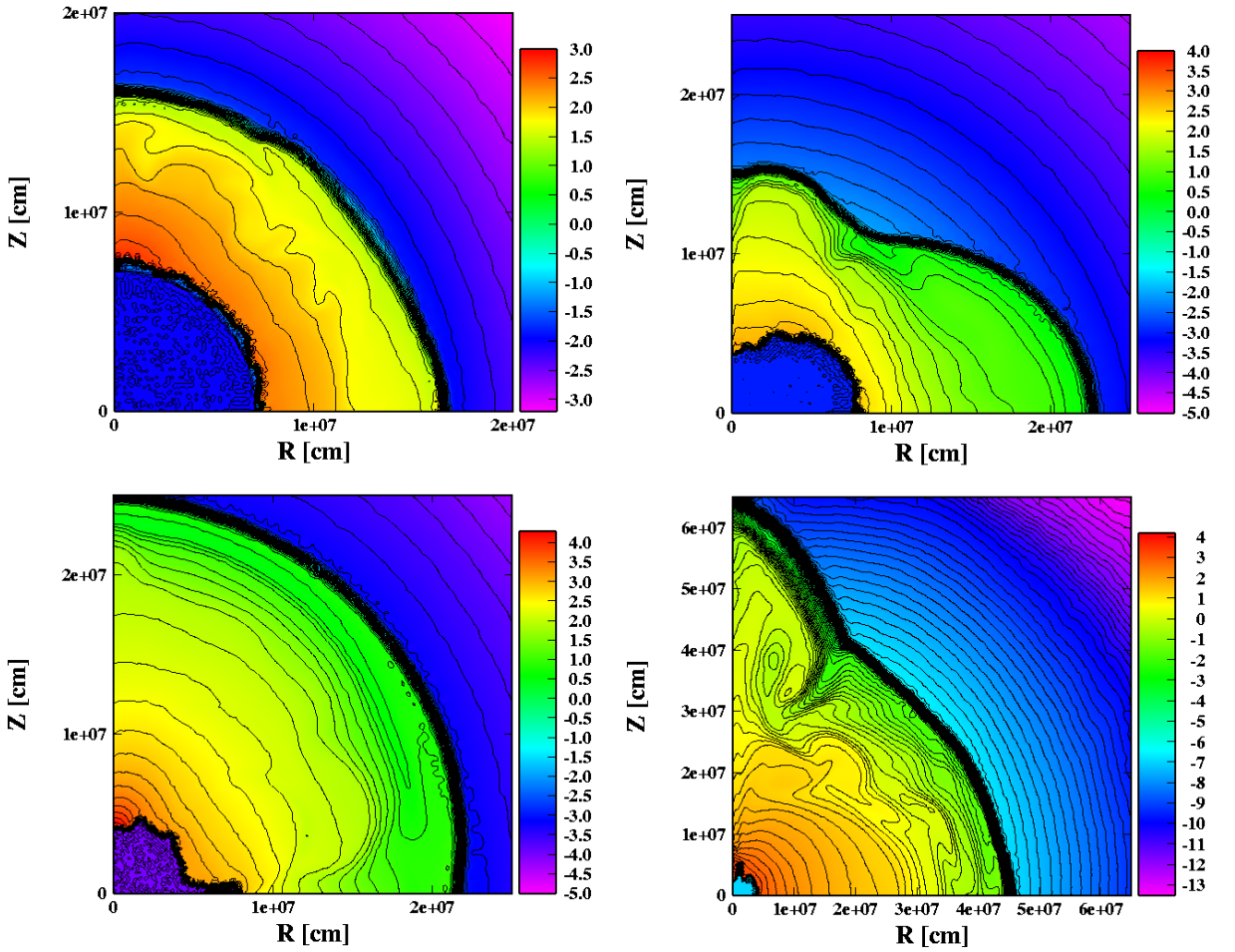

Fig. 9.— The heating rates outside the neutrino sphere for models SSL7 (upper left), MSL4 (upper right), MSS4 (lower left), MCS1 (lower right). All the figures show color-coded contour plots for the logarithm of the heating rate Q_ν^+ (MeV nucleon^{-1} s^{-1}). The neutrino sphere and the stalled shock are seen as thick black lines separating bright-color from dark-color regions. Note that the value within the neutrino sphere is artificially modified so that it has dark colors, which has no physical meanings.

3.4. Anisotropic Neutrino Radiation from the Deformed Neutrino Sphere.

Based on the neutrino spheres obtained in the previous section, we will estimate the heating rates outside the neutrino sphere. This is admittedly a very crude estimate, since it is pointed out (Liebendörfer et al. 2001; Thompson, Burrows, & Pinto 2003) that the net heating, the heating minus cooling, becomes positive $\sim 50 - 100$ msec after the shock stagnation. In this respect, we confirmed that the cooling dominates over the heating also in our models. Since our calculations ended before the heating dominates over the cooling, it is impossible to estimate the location of the gain radius, beyond where the heating dominates over the cooling. Here it is noted that the contrast of the heating to the cooling is found to be similar in our short simulation runs. Thus, the gain radius should be also deformed in the later phase. If this feature lasts in the later phase, the bare heating rate discussed in the following, will help to understand the net neutrino heating. Hence, bearing this caveat in mind, we study the bare heating rate for the final configurations (several tens msec after the bounce) in our simulations.

We follow the same procedure taken in Kotake et al. (2003). It is assumed that neutrinos are emitted isotropically from each point on the neutrino sphere and stream freely later on. Then the heating rate at a given point outside the neutrino sphere can be found by summing up all the rays gathering to the point from the neutrino sphere. We summarize it again here for convenience.

The heating of the gas outside the neutrino sphere by electron neutrinos proceeds via the charged current interaction process:

$$\nu_{\rm e} + n \rightarrow p + e^{-}. \tag{11}$$

With the typical cross section,

$$\sigma_0 = \frac{4\ G_{\rm F}^2\ (m_{\rm e}c^2)^2}{\pi\ (\hbar c)^4}, \tag{12}$$

where $G_{\rm F}$ is the universal Fermi constant and $m_{\rm e}$ is the rest mass of electron, the cross section of (11) to the leading order is expressed as

$$\sigma_0{}^{(\rm abs)} = \sigma_0 \Big(\frac{1+3g_{\rm A}^2}{4}\Big)\Big(\frac{\epsilon_\nu}{m_e c^2}\Big)^2, \tag{13}$$

where $g_{\rm A}$ is the axial-vector coupling constant (~ -1.26) and ϵ_ν is the neutrino energy.

The heating rate (Janka 2001) is given as

$$Q^+{}_\nu = \int \sigma_0{}^{(\rm abs)}\ c\ n_{\rm n}\epsilon_\nu \frac{d^2 n_\nu}{d\epsilon_\nu d\Omega} d\epsilon_\nu d\Omega, \tag{14}$$

where $d^2n_\nu/(d\epsilon_\nu\ d\Omega)$ is related to the neutrino distribution in the phase space $f(\epsilon_\nu, \Omega)$:

$$\frac{d^2n_\nu}{d\epsilon_\nu d\Omega} = \frac{1}{(hc)^3} f_\nu(\epsilon_\nu, \Omega)\ \epsilon_\nu^2. \tag{15}$$

Introducing Eqs. (13), (15) into (14) yields

$$Q^+{}_\nu = \frac{3\alpha^2+1}{4} \frac{\sigma_0\, c\, n_{\rm n}}{(hc)^3} \frac{\langle\epsilon_\nu^2\rangle}{(m_{\rm e}c^2)^2}\ \Omega \int d\epsilon_\nu\ \epsilon_\nu^3\, f_\nu(\epsilon_\nu)\,, \tag{16}$$

where

$$\langle\epsilon_\nu^2\rangle = \int d\epsilon_\nu\, \epsilon_\nu^5\, f_\nu(\epsilon_\nu) \Big(\int d\epsilon_\nu\, \epsilon_\nu^3 f_\nu(\epsilon_\nu) \Big)^{-1}. \tag{17}$$

As stated, the neutrino emission from each point on the neutrino sphere is assumed to be isotropic and take a Fermi distribution with a vanishing chemical potential. Eq. (16) is expressed with the local neutrino flux, j_ν, which is calculated from the neutrino luminosity obtained in the simulations:

$$Q^+{}_\nu = \frac{(3\alpha^2+1)}{4\,\pi} \sigma_0 n_{\rm n} \frac{\dfrac{F_5(0)}{F_3(0)}(kT_\nu)^2}{(m_e c^2)^2}\ j_\nu\, \Omega, \tag{18}$$

where we used the relations,

$$\langle\epsilon_\nu^2\rangle = F_5(0)/F_3(0)(kT_\nu)^2, \tag{19}$$

with $F_5(0)$ and $F_3(0)$ being the Fermi integrals and

$$\begin{aligned} j_\nu &= c\, \frac{2\pi}{(hc)^3} \int d\epsilon_\nu\, \epsilon_\nu^3\, f_\nu(\epsilon_\nu) \int_0^1 d\mu\, \mu \\ &= c\, \frac{\pi}{(hc)^3} \int d\epsilon_\nu\ \epsilon_\nu^3\, f_\nu(\epsilon_\nu). \end{aligned} \tag{20}$$

The solid angle Ω is calculated by numerical integrations.

In Figure 9, the color contours of the heating rate for the representative models are given. For faster rotation models, the neutrino emission becomes anisotropic, while the neutrino emission for model SSL7 is almost isotropic. It is found that the anisotropy parameter $R_{\rm anisotropy}$ is generally greater than unity for the fast rotation models, while it is almost unity for model SSL7. The reason for the former is that the neutrino temperatures at the rotational axis are generally higher than on the equatorial plane as mentioned before. In addition, the solid angle is larger for the vicinity of the rotational axis, since the radii of the neutrino spheres tend to be smaller near the rotational axis. These effects make the neutrino heating near the rotational axis more efficient.

In some of our models, the stronger magnetic fields exceed the QED critical value $B_{\rm QED} = 4.4 \times 10^{13}$ G, above which the neutrino reactions are affected by parity-violating corrections of weak interactions (Horowitz & Li 1998; Arras & Lai 1999). The correction to the cross section of electron neutrino absorption on neutron, for example, is proportional to $\int d\Omega\ \hat{\boldsymbol{n}} \cdot \hat{\mathbf{B}}$ at the tree level. Here $\hat{\boldsymbol{n}}$, $\hat{\mathbf{B}}$ are the unit vector in the direction of the incoming neutrinos and along the magnetic field, respectively. Since magnetic fields are nearly toroidal with axial symmetry in this study, this correction is negligible in our models.

Table 4. Results of the Heating Rate Analysis.

Model	$R_\nu{}^{\rm p}$ (km)	$R_\nu{}^{\rm e}$ (km)	$T_\nu{}^{\rm p}$ (MeV)	$T_\nu{}^{\rm e}$ (MeV)	$R_{\rm anisotropy}$	L_ν (10^{52} erg s^{-1})
SSL7	71.4	71.4	3.39	3.49	0.89	2.19
MSL4	36.2	76.4	7.22	3.63	1.85	1.28
MSL2	37.5	79.8	7.07	3.58	2.11	1.38
MSL1	36.2	81.5	6.66	3.33	2.41	1.64
MSS4	38.9	74.7	7.31	2.30	4.67	2.29
MSS2	40.6	78.1	7.81	2.59	4.90	2.05
MSS1	40.2	48.5	6.70	6.71	5.54	1.21
MCS4	19.8	40.1	7.17	2.59	2.27	2.05
MCS2	20.0	42.9	6.00	6.97	1.92	0.47
MCS1	21.2	34.9	4.83	5.02	0.92	0.39

Note. — $R_\nu{}^{\rm e}$ and $R_\nu{}^{\rm p}$ are the distances from the center to the neutrino sphere, $T_\nu{}^{\rm e}$ and $T_\nu{}^{\rm p}$ are the neutrino temperatures on the neutrino sphere, on the equator and the rotational axis, respectively. $R_{\rm anisotropy} = Q_\nu^{+p}/Q_\nu^{+e}$ is the ratio of heating rates at the rotational axis to that on the equator and represents the degree of the anisotropy of neutrino heating. Here Q_ν^{+p}, Q_ν^{+e} are the heating rates on the rotational axis and the equator and are estimated at the nearest grid to the neutrino sphere. L_ν is the neutrino luminosity.

3.5. Convective Stability Analysis

As known well (eg., Herant et al. (1994); Janka & Müller (1994); Burrows & Fryxell (1993)), convections behind the shock increase the efficiency of neutrino heating and are helpful for explosions. As a driving force of the instabilities, previous studies are mainly focused on the negative gradient of entropy and lepton fraction and/or rotation (see, however, for the instability induced by the magnetic fields, Thompson & Murray 2001; Akiyama et al. 2003). Here we pay attention to the effect of magnetic fields on the convective instability. In particular, we investigate the toroidal magnetic fields, since the toroidal component is likely to be dominant. From the neutrino heating analysis, it is indicated that matters behind the shock wave can be heated preferentially near the rotational axis due to the anisotropic neutrino heating induced by rotation. We estimate the effects of the magnetic buoyancy, which is produced by a small upward displacement of the toroidal magnetic loops against the gravity along the rotational axis. It is noted that we discuss the adiabatic linear stability and neglect the neutrino heating/cooling here, since they are minor effects outside the neutrino sphere. The Solberg - Høiland criterion, which expresses the convective instabilities for the rotating stars (Tassoul 1978; Janka & Keil 1997), is modified in order to include the effect the magnetic buoyancy as follows

$$\begin{aligned} & \frac{1}{X^3}\frac{dj_{\rm z}{}^2}{dX} + \frac{\vec{a}}{\rho}\cdot\Big[\Big(\frac{\partial\rho}{\partial S}\Big)_{P,Y_l}\mathrm{grad}\ S + \Big(\frac{\partial\rho}{\partial \mathrm{Y}_l}\Big)_{\mathrm{P},S}\mathrm{grad}\ \mathrm{Y}_l\Big] + \frac{\mathrm{g_z}\ \mathrm{v_A^2}}{\gamma\ \mathrm{c_s^2}}\frac{\mathrm{d}}{\mathrm{dZ}}\ln\Big(\frac{\mathrm{B}_\phi}{\rho}\Big) \\ \equiv\ & N_{\rm rot} + N_{\rm LD} + N_{\rm mag} \equiv N_{\rm tot} < 0. \end{aligned} \tag{21}$$

Here $j_{\rm z}$ is a specific angular momentum of a fluid element, X is the distance from the rotational axis, Y_l is the lepton fraction, S is the entropy per nucleon, a is the acceleration due to the sum of the gravitation and centrifugal forces, $g_{\rm z}$ is the gravitation along the rotation axis, $c_{\rm s}$ is the sound speed, $v_{\rm A} = B/\sqrt{4\pi\rho}$ is the Alfvén speed, and $\gamma = (\partial \ln p/\partial \ln \rho)_{\rm s}$ is the adiabatic index. The terms in the bracket of Eq. (21) represent the Ledoux criterion for non-rotating stars. The third term represents the magnetic buoyancy (Acheson 1979). The growth timescale τ, is given by equating the left hand side of Eq. (21) with τ^{-2} which is an extention of the Brunt-Väisälä frequency.

We first discuss model SSL7 which is based on the recent stellar evolution calculation (Heger et al. 2003). The lower left panel in Figure 10 shows the contour plot of $N_{\rm tot}$. The regions inside the protoneutron star ($R \sim 30$ km) are stabilized by the positive gradient of $N_{\rm LD}$. On the other hand, the regions just outside the protoneutron star in the vicinity of the equatorial plane are found to convectively unstable by the negative lepton gradient caused by the neutrino emission. Since the specific angular momentum reaches its maximum and its derivative respective to X is small there, the negative lepton gradient dominates over the stabilizing contribution from $N_{\rm rot}$. The timescale of the growth of the instability is ~ 10

msec, which is estimated by $2\pi/\sqrt{N_{\rm tot}}$. From the upper panel of Figure 10, there are regions where the specific angular momentum decreases outwards from the rotational axis. In fact, the convectively unstable regions by the negative gradient of $N_{\rm rot}$ are found in the lower left panel of Figure 10 (see the regions with the dark color within the radius of 100 km). The timescale of the growth of the instability is ~ 10 msec. From the lower right panel of Figure 10, the convective motions in the corresponding regions can be seen to be developing. It should be because the final times of our calculations (~ 50 msec after core bounce) are longer than the growth timescale of ~ 10 msec.

The negative values of $N_{\rm mag}$ are found to be located at a radius of ~ 10 km near the rotational axis in the models with the strongest magnetic fields. In the region, the toroidal magnetic fields have a steeper negative gradient than other regions. However, the region is below the surface of the protoneutron star. As a result, the positive gradient of entropy and lepton fraction stabilizes the fluid. Thus, no convectively unstable regions formed by the magnetic buoyancy are found in our models. However, this situation does not mean that the effects of the magnetic field on the instability are not important. We discuss the importance of the magnetorotational instability in the following.

As discussed by Balbus & Hawley (1998); Akiyama et al. (2003); Proga, MacFadyen, Armitage, & Begelman (2003), the magnetorotational instability (MRI) induced by the axisymmetric perturbations is an important gradient, which amplifies the magnetic fields. However, such amplification does not occur in this study. This is because the magnetic fields in our models are almost purely toroidal with the assumption of axial symmetry. This situation leads us to discuss the MRI induced by the nonaxisymmetric perturbations. From the left side panels of Figure 6. the negative gradient of the angular velocity $d\Omega/dX < 0$ can be seen, where Ω is the angular velocity and X is the distance from the rotational axis. Such regions are known to be unstable to the non-axisymmetric perturbation (Balbus & Hawley 1992). The characteristic timescale for the maximum growth rate of the instability is given as $\tau_{\rm MRI} = 4\pi(d\Omega/d\log X)^{-1}$. In Figure 11, the contour plots of the $\tau_{\rm MRI}$ for the models with the strongest magnetic fields are presented. From the figure, the timescales are found to be $\sim O(10)$ msec near the vicinity of the rotational axis. It suggests that the MRI induced by the non-axisymmetric perturbation can grow for the prompt-shock time scale. Combined with the anisotropic neutrino radiation, which heats matter near the rotational axis preferentially, the growth of the instability may enhance the heating near the axis.

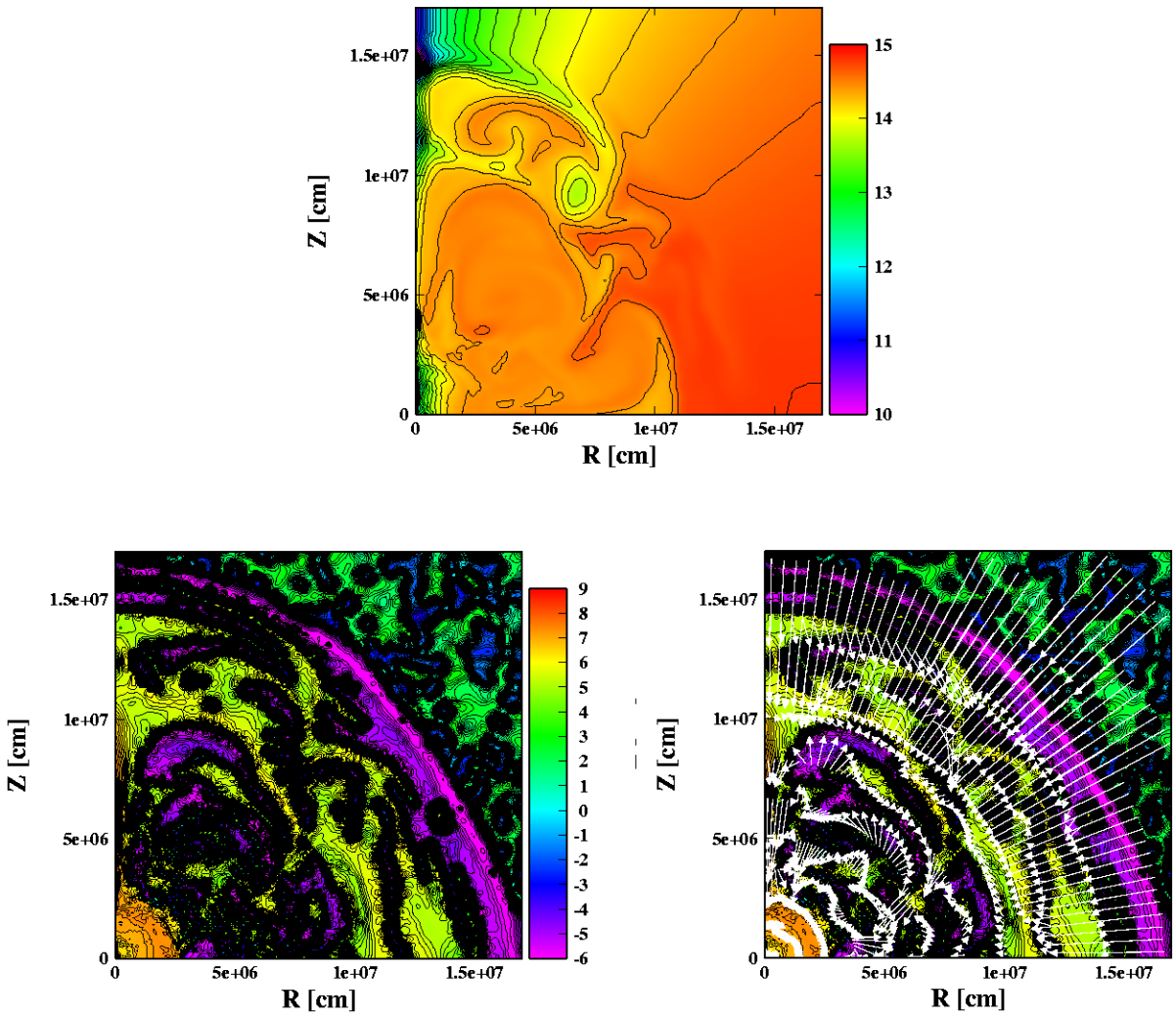

Fig. 10.— Convectively unstable regions in model SSL7. In the upper center panel, the color contour of the logarithm of the specific angular momentum, $j(\mathrm{cm}^2\ \mathrm{s}^{-1})$, is shown. The lower panels show the color contour of the sum of terms, N_{tot} (s^{-2}), in Eq. (21). Note in the lower panels that if the value of the color scale is given as x, $x/|x| \times 10^{|x|}$ expresses the values of N_{tot}. Thus, the regions with the darker colors are convectively unstable. The velocity fields, which show the convective motions, are presented in the lower right panel.

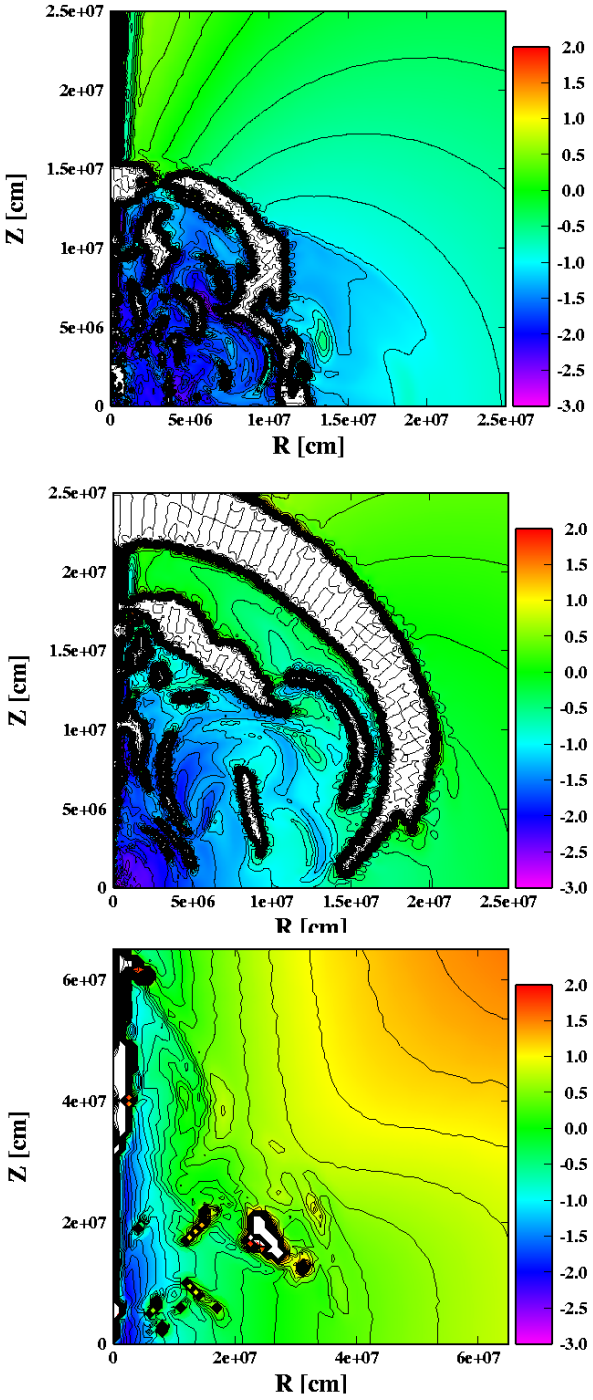

Fig. 11.— The magnetorotational unstable regions by the non-axisymmetric perturbation for models MSL1 (top), MSS1 (middle), and MCS1 (bottom). The contour plots show the logarithm of the growth timescale of the MRI, $\tau_{\rm MRI}$ (s). The white color in the panels represents the stable regions against the MRI.

4. Discussions

In our simulations, only electron neutrinos are treated approximately. Since all the computations are limited to rather early phases ($\sim$ 50 msec after the core bounce), it may not be a bad approximation. However, this is certainly a limitation to the study of the later phases which are more important for the neutrino heating mechanism. As already mentioned, if we take into the cooling, no heating region is found at these early times. As shown, for example, by Thompson, Burrows, & Pinto (2003), the heating region or (the gain region) appears more than 50 $\sim$ 100 msec after core bounce. Hence, our estimate of anisotropic neutrino heating is admittedly a bold extrapolation to the later phases, which we have not computed yet. Although we hope that the general features obtained in that way will be taken over later on, this needs further investigation. As for the initial configurations of the toroidal magnetic fields, we assume that they have the same profile as the rotation. The assumption may not be unnatural because the angular momentum transfer in quasistatic stellar evolution is tightly connected to the formation of the magnetic fields (Spruit 2002). However, multidimensional and self-consistent calculations are required to be done for the understanding of the magnetorotational evolution of supernova progenitors.

When we estimate the growth timescale $\tau_{\rm MRI}$, the gradients of lepton, entropy and specific angular momentum are excluded. Thus the timescale represents a lower limit. In order to investigate the growth of the instability, we are preparing for the 3D MHD simulations (H. Sawai et al. 2004, in preparation).

Finally we briefly discuss the difference between our results and the recent studies including rotation. Ott et al. (2003) performed a large number of 2D purely-hydrodynamic calculations employing a realistic equation of state (EOS) while neutrino transfer and microphysics are not treated. They employed the Lattimer-Swesty EOS, which is softer at nuclear density than the one we employed. The qualitative features of the hydrodynamics induced by rotation are consistent with ours. On the other hand, the quantitative comparisons of their results with ours are not straightforward. This is because the neutrino cooling incorporated in this study should make the major differences between our results and their adiabatic simulations. By employing the Lattimer-Swesty EOS, we are now investigating how the features of EOS's result in the differences of the dynamics, while fixing the microphysics. This will be presented in our forthcoming paper (Kotake et al. 2004). Fryer & Heger (2000) performed 2D rotational core-collapse simulations, treating neutrino transfer by the flux-limited, gray diffusion approach. Their conclusions that convection occurs near the rotational axis is consistent with ours. More recent work by Fryer & Warren (2003), which extended the study by Fryer & Heger (2000) to the 3D calculations, refers to the deformation of the neutrino sphere induced by rotation. Their results that the neutrino spheres are deformed to be oblate

are similar to our results. However, little effect of neutrino anisotropy on the explosion are found. This is probably their models explode in the prompt-shock timescale. Buras et al. (2003) did the first two-dimensional rotational core-collapse simulation with a Boltzmann solver for the neutrino transport (see also Müller et al. 2003). Their calculation should be the most advanced study to date of the effects of rotation on the core collapse supernovae. It is noted that even in their model no successful explosion is obtained. However their treatment of neutrino transfer is along the radial rays and is not fully two-dimensional (e.g., Livne et al. (2003)). As we emphasize, the neutrino heating in the lateral direction should be important. Thus we think that their results have not excluded the possibility of anisotropic neutrino-driven explosion considered here and that further investigations are necessary.

5. Conclusion

We performed a series of hydrodynamic simulations of magnetorotational core collapse, in which we employed the realistic equation of state based on the relativistic mean field theory. The electron captures and the neutrino transport were simplified via the neutrino leakage scheme. The recent stellar evolution calculations suggest that the toroidal components of the magnetic field of are stronger than the poloidal ones at the presupernova stage. Thus, we studied the effect of the toroidal magnetic fields on the anisotropic neutrino radiation and convection, in which the strength and the distribution of the toroidal magnetic fields are changed in a parametric way. In addition, changing the initial rotation profiles and strength, and degree of differential rotation, we computed 10 models. Then we studied the anisotropic neutrino radiation from the deformed neutrino sphere and estimated the convectively unstable regions. As a result, we found the following.

(1) By the inclusion of the toroidal magnetic fields, the shapes of the shock wave tend to become more oblate for the models, whose profiles of rotation and the magnetic field are shell-type, than the corresponding models without the magnetic fields. This is because the toroidal magnetic fields with the shell-type rotation push the matter rather parallel to the equatorial plane. On the other hand, the shapes of the shock wave become more prolate for the models, whose profiles of rotation and magnetic field are cylindrical, than the corresponding models without the magnetic fields. For the models, the magnetic fields are confined to the small region behind the shock wave and push the shock wave, which acts as strong as the matter pressure. Between the spherical model and the model based on the recent stellar calculation including rotation and magnetic fields, no significant differences in the hydrodynamic features are found.

(2) As the final shapes of the shock wave are affected by the magnetic fields, the shapes

of the neutrino sphere become more oblate for the models whose profiles of rotation and magnetic field are shell-type, in contrast, more prolate for the models whose profiles of rotation and magnetic field are cylindrical, than the corresponding models without the magnetic fields. Although the magnetic fields affect the shapes of the neutrino sphere, the shapes are found to be predominantly determined by rotation over the wide range of the initial field strength. The anisotropic neutrino radiation, and, thus, heating are commonly found in the fast rotation models. Matter near the rotational axis is heated more intensely than in the equatorial region. This is mainly because the neutrino temperatures are higher near the rotational axis. In addition, the radius of the neutrino sphere tends to be smaller in the vicinity of the rotational axis. As a result, the solid angle of the neutrino sphere is larger seen from the rotational axis. These two effects make the neutrino heating near the rotational axis more efficient.

(3) In the model corresponding to the recent stellar evolution calculation, the convectively unstable regions appear at the surface of the protoneutron star in the vicinity of the equatorial plane and behind the stalled shock, induced by the negative lepton and entropy gradient, respectively. In addition, another convective regions prevail near the rotational axis from the surface of the protoneutron up behind the radius of ~ 100 km. This is induced by the negative gradient of the specific angular momentum. This may be another cause of the anisotropic neutrino heating.

(4) In some models with the strongest magnetic fields, the regions with the negative gradient of the angular velocity are found near the rotational axis. In such regions, the magnetorotational instability induced by the nonaxisymmetric perturbations is expected to develop, since the growth timescales are within the prompt shock timescale. Combined with the anisotropic neutrino radiation, which heats matter near the rotational axis preferentially, the growth of the instability may enhance the heating near the axis. This might suggest that the magnetar formation is accompanied by the jet-like explosion.

As stated earlier, our simulations are crude in the treatment of microphysics compared with recent spherical models. This may be justified as long as we study the earlier phase in the prompt explosion timescale. We are currently developing a two-dimensional neutrino transfer code, which will be indispensable for the study of the later phase (K. Kotake et al. 2003 in preparation).

K.K is grateful to K. Sumiyoshi for providing us with the tabulated equation of state, which can be handled without difficulties. The numerical calculations were partially done on the supercomputers in RIKEN and KEK (KEK supercomputer Projects No.02-87 and No.03-92). This work was partially supported by Grants-in-Aid for the Scientific Research

from the Ministry of Education, Science and Culture of Japan through No.S 14102004, No. 14079202, and No. 14740166.

REFERENCES

Acheson, D. J. 1979, Sol. Phys., 62, 23

Akiyama, S., Wheeler, J. C., Meier, D. L., & Lichtenstadt, I. 2003, ApJ, 584, 954

Ardeljan, N. V., Bisnovatyi-Kogan, G. S., & Moiseenko, S. G. 2000, A&A, 355, 1181

Arras, P. & Lai, D. 1999, Phys. Rev. D, 60, 43001

Bisnovatyi-Kogan, G. S. & Ruzmaikin, A. A. 1976, Ap&SS, 42, 401

Bludman, S. A., Lichtenstadt, I., & Hayden, G. 1982, ApJ, 261, 661

Balbus, S. A. & Hawley, J. F. 1998, Reviews of Modern Physics, 70, 1

Balbus, S. A. & Hawley, J. F. 1992, ApJ, 400, 610

Buras, R., Rampp, M., Janka, H.-T., & Kifonidis, K. 2003, Phys. Rev. Lett., 90, 241101

Burrows, A & Thompson, T. A. To be published as a Chapter in "Core Collapse of Massive Stars," ed. C.L. Fryer, Kluwer Academic Publ, (astro-ph/0211404)

Burrows, A., & Fryxell, B. 1993, ApJ, 418, L33

Duncan, R. C. & Thompson, C. 1992, ApJ, 392, L9

Epstein, R. I. & Pethick, C. J. 1981, ApJ, 243, 1003

Fryer, C,L., & Heger, A. 2000, ApJ, 541, 1033

Fryer, C.L, & Warren, M, S, 2003, accepted by ApJ.

Guseinov, O. H., Yazgan, E., Ankay, A., & Tagieva, S. O. 2003, International Journal of Modern Physics D, 1, 1

Heger, A., Woosley, S. E., Langer, N., and Spruit, H. C. 2003, to appear in Proc. IAU 215 "Stellar Rotation", (astro-ph/0301374)

Herant, M., Benz, W., Hix. W.R., Fryer, C,L., & Colgate, S.A. 1994, ApJ, 435, 339

Horowitz, C. J. & Li, G. 1998, Physical Review Letters, 80, 3694

Janka, H.-T. 2001, A&A, 368, 527

Janka, H-T., Keil, W. in Supernovae and Cosmology, Proc. of the Colloquium in Honor of Prof. G. Tammann, Augst, Switzerland, June 13, 1997.

Janka, H-T., & Müller, E. 1996, A&A, 290, 496

Kotake, K., Yamada, S., & Sato, K. 2003, ApJ, 595, 304

Kotake, K., Yamada, S., & Sato, K. 2003, Phys. Rev. D, 68, 044023

Kotake, K., Yamada, S., Sato, K., Sumiyoshi, K., Ono, H., and Suzuki, H. 2004, Phys. Rev. D, in press.

Livne, E., Burrows, A., Walder,R., Lichtenstadt, I., and Thompson, T.A. 2003, submitted to ApJ

LeBlanc, J.M., & Wilson, J.R. 1970, ApJ, 161 ,541

Liebendörfer, M., Mezzacappa, A., Thilemann, F.-K., Messer, O.E.B., Hix, W.R., and Bruenn, S.W. 2001, Phys. Rev. D, 63, 103004

Liebendörfer, M., Rampp, M., Janka,H.-T., Mezzacappa, A. 2003, submitted to ApJ

Meier, D. L., Epstein, R. I., Arnett, W. D., & Schramm, D. N. 1976, ApJ, 204, 869

Mönchmeyer, R, M., & Müller, E. 1989, in NATO ASI Series, Timing Neutron Stars, ed. H. Ögelman & E.P.J van der Heuvel (New York: ASI)

Müller, E. & Hillebrandt, W. 1979, A&A, 80, 147

Müller, E. et al. 2003, submitted to ApJ

Nagataki, S., Hashimoto, M., Sato, K., & Yamada, S. 1997, ApJ, 486, 1026

Nagataki, S. 2000, ApJS, 127, 141

Ott, C, D., Burrows, A., Livne, E., & Walder, R, 2003, submitted to ApJ, (astro-ph/0307472)

Parker, E. N. 1979, Cosmological magnetic fields: The origin and their activity (Oxford, Clarendon Press)

Proga, D., MacFadyen, A. I., Armitage, P. J., & Begelman, M. C. 2003, ApJ, 599, L5

Pun, C. S. J., & The Supernova Intensive Studies (SNIS) Collaboration. 2001, AAS Meeting, 199, 94. 02

Rampp, M. & Janka, H.-T. 2000, ApJ, 539, L33

Shen, H., Toki, H., Oyamatsu, K., Sumiyoshi, K. 1998, Nuclear Physics, A637, 43, 109, 301

Shimizu, T. M., Ebisuzaki, T., Sato, K., & Yamada, S. 2001, ApJ, 552, 756

Spruit, H. C. 2002, A & A, 381, 923

Symbalisty, E. 1984, ApJ, 285, 729

Stone, J. M. & Norman, M. L. 1992, ApJS, 80, 791

Tassoul, J.-L. 1978, Theory of Rotating Stars (Princeton: Princeton Univ. Press)

Thompson, C. & Murray, N. 2001, ApJ, 560, 339

Thompson, T. A., Burrows, A., & Pinto, P. A. 2003, ApJ, 592, 434

van Riper, K. A. & Lattimer, J. M. 1981, ApJ, 249, 270

van Riper, K. A. 1982, ApJ, 257, 793

Woosley, S. E. & Weaver, T. A. 1995, private communication

Wang, L., Wheeler, J. C., Li, Z., & Clocchiatti, A. 1996, ApJ, 467, 435

Wang, L., Howell, D. A., Höflich, P., & Wheeler, J. C. 2001, ApJ, 550, 1030

Wang, L., et al. 2002, ApJ, 579, 671

Yamada, S. & Sato, K. 1994, ApJ, 434, 268

Yamada, S. & Sawai, H. 2003, submitted to ApJ

Zhang, B. & Harding, A. K. 2000, ApJ, 535, L51